Pan-Spectral Observing System Simulation Experiments of Shortwave Reflectance and Longwave Radiance for Climate Model Evaluation

Daniel R. Feldman[1, †] William D. Collins[1,2], John L. Paige[1]

[1] Lawrence Berkeley National Laboratory, Earth Sciences Division

[2] University of California-Berkeley, Department of Earth and Planetary Science

[†] Corresponding Author:

drfeldman@lbl.gov

1 Cyclotron Road - MS 74R-316C

Berkeley, CA 94720, USA

Revised Submission for *Geoscientific Model Development*

Abstract

Top-of-atmosphere spectrally-resolved shortwave reflectances and longwave radiances describe the response of the Earth's surface and atmosphere to feedback processes and human-induced forcings. In order to evaluate proposed long-duration spectral measurements, we have projected 21st Century changes from the Community Climate System Model (CCSM3.0) conducted for the Intergovernmental Panel on Climate Change (IPCC) A2 Emissions Scenario onto shortwave reflectance spectra from 300 to 2500 nm and longwave radiance spectra from 2000 to 200 cm^{-1} at 8 nm and 1 cm^{-1} resolution, respectively. The radiative transfer calculations have been rigorously validated against published standards and produce complementary signals describing the climate system forcings and feedbacks. Additional demonstration experiments were performed with the MIROC5 and HadGEM2-ES models for the Representative Concentration Pathway 8.5 (RCP8.5) scenario. The calculations contain readily distinguishable signatures of low clouds, snow/ice, aerosols, temperature gradients, and water vapour distributions. The goal of this effort is to understand both how climate change alters reflected solar and emitted infrared spectra of the Earth and determine whether spectral measurements enhance our detection and attribution of climate change. This effort also presents a path forward to understand the characteristics of hyperspectral observational records needed to confront models and inline instrument simulation. Such simulation will enable a diverse set of comparisons between model results from coupled model intercomparisons and existing and proposed satellite instrument measurement systems.

1. Introduction

The spectrally-integrated upwelling top-of-atmosphere radiant energy field comprises the Earth system's total energy balance, and comprehensive comparisons of modelled Outgoing Longwave Radiation (OLR) and albedo with observationally-based estimates of these quantities have led to important constraints on climate models [e.g., Morcrette, 1991; Kiehl et al., 1994]. The spectrally resolved energy field spans an additional dimension that contains information regarding the processes that govern that balance. Moreover, it has been demonstrated that infrared spectra contain important information that can be used to test climate models [e.g., Goody et al., 1998], primarily because the spectral signatures of individual forcings and feedbacks can be readily separated, detected, and quantified. Recent work by Roberts et al. [2011] suggest that shortwave spectra also contain independent information about processes that contribute to albedo. Although the separability of processes that contribute to albedo from these spectra has not been addressed formally, Jin et al [2011] showed the utility of shortwave spectral fingerprints which may be extended to consider spectral separability.

This has motivated the implementation of Observing System Simulation Experiments (OSSEs) based on climate models as a means for exploring the utility of well-posed comparisons between models and measurements. OSSEs are well-established techniques for evaluating the scientific and operational value of new instruments proposed for meteorological applications [Arnold and Dey, 1986]. The role of OSSEs for climate science is less mature than that of the application to short-term weather forecasting for which they were originally developed. The decadal length of climate studies and the necessarily long measurement records that are needed to confront how models predict climate change motivate the development of climate model OSSEs. The forward evaluation of remote sensing signal sensitivity to uncertain model parametrisations and/or global climate sensitivity contributes to the determination of the value of certain types of remote sensing measurements where the underlying climate signal from the

63 model is known. To that end, it has been recently noted by the Intergovernmental Panel on
64 Climate Change (IPCC) that instrument simulators are valuable in that they can obviate
65 inconsistencies between models and measurements [Flato et al., 2013].
66
67 Several investigations have explored direct comparisons between measurements from a variety
68 of existing satellite-based instruments and simulations of those measurements based on various
69 climate model integrations. For example, community-wide efforts have led to the establishment
70 of the Cloud Feedback Model Intercomparison Project Observational Simulator Package
71 (COSP) [Bodas-Salcedo et al., 2011], enabling inline instrument simulations for existing
72 missions including the International Satellite Cloud Climatology Project (ISCCP), the MODerate
73 Resolution Imaging Spectroradiometer (MODIS), CloudSat, and Cloud-Aerosol Lidar and
74 Infrared Pathfinder Satellite Observation (CALIPSO). Results from COSP based on models run
75 in historical mode are then compared to existing measurement records to identify model biases
76 (e.g., Kay et al. [2012]; Pincus et al. [2012]).
77
78 Additionally, there have been efforts to explore how hyperspectral measurements can be
79 utilised for facile measurement-model intercomparison. Huang et al. [2007; 2010a] and Leroy et
80 al. [2008] examined longwave measurements and radio occultation simulations in detail and
81 have compared the spectral signatures of variations in lapse rate, water vapour, and cloud
82 radiative effects (CREs). The discrepancies in measured and modelled spectra suggest that the
83 agreement in measured and modelled OLR is a result of compensating errors between
84 temperature, water vapour, and cloud structure in the models.
85
86 Feldman et al. [2011a; 2011b; 2013] developed climate OSSEs with shortwave spectra. These
87 works showed utility of shortwave spectra for detecting climate change, and found that

shortwave measurements are more sensitive to low clouds and changes in frozen surface extent than are longwave spectral measurements.

Despite the potential utility of using visible, near-infrared, and infrared measurements, the simultaneous utilisation of shortwave reflectance and longwave radiance spectra to address climate change questions has not been explored in detail to date, despite the numerous studies based on coincident observations of broadband OLR and albedo [e.g., [Kiehl and Trenberth, 1997; Hansen et al., 2005; Wielicki et al., 2006; Loeb et al., 2009]. The combination of shortwave and longwave hyperspectral measurements could potentially be quite useful in addressing fundamental and unanswered questions related to shortwave cloud and ice feedbacks while simultaneously describing the temperature and water vapour structure of the atmosphere. The ultimate goal of this research area is to develop rigorous observational tests for climate models with a particular focus on using measurements to constrain climate model sensitivity.

Existing hyperspectral infrared measurement systems including the Atmospheric Infrared Sounder (AIRS) [Aumann et al., 2003] and the Infrared Atmospheric Sounding Interferometer (IASI) [Siméoni et al., 1997] can be considered as strong observational constraints. Moreover, hyperspectral shortwave measurements are available from the SCanning Imaging Absorption SpectroMeter for Atmospheric CHartographY (SCIAMACHY) [Bovensmann et al., 1999], and these extensive data records could be useful for measurement-model intercomparison.

This paper presents a versatile tool for simulating spectrally resolved measurements from the near-UV (300 μm) to the far-infrared (50 μm) and discusses how these measurements can be used to generalise existing OSSE efforts. It demonstrates the rigorous radiometric validation needed to establish comprehensive science traceability studies for planned instruments such

114 those recommended by the National Research Council's Decadal Survey including CLimate
115 Absolute Radiance and Refractivity Observatory (CLARREO) [Wielicki et al., 2013] and
116 GEOstationary Coastal and Air Pollution Events (GEO-CAPE) [Space Studies Board, 2007].
117 Additionally, the pan-spectral OSSE may be utilised to develop climate model observational
118 tests for evaluating results reported to the Coupled Model Intercomparison Project – Phase 5
119 (CMIP5) [Taylor et al., 2012] and Phase 6 (CMIP6) [Meehl et al., 2014].
120
121 **2. Methodology**
122 Following Feldman et al. [2011a], we present OSSE calculations of shortwave spectral
123 reflectance and longwave spectral radiance that simulates spectral measurements based on the
124 climate projections conducted with Community Climate System Model, Version 3.0 (CCSM3)
125 integrations [Collins et al., 2006a; Meehl et al., 2006]. The spectral calculations are performed
126 with the MODerate Resolution TRANsmission (MODTRAN^{TM}) radiative transfer code [Berk et al.,
127 2005]. The shortwave and longwave spectra are calculated from 0.3 to 2.5 μm (33333 to
128 4000 cm^{-1}) at a 15 cm^{-1} native resolution, and from 5 to 50 μm (2000 to 200 cm^{-1}) at a 1 cm^{-1}
129 native resolution, respectively. The calculations produce top-of-atmosphere (TOA) radiance
130 spectra and upwelling and downwelling direct and diffuse spectral flux (irradiance) fields at each
131 vertical level of CCSM3.
132
133 The fields produced in CCSM3 integrations include vertical profiles of atmospheric
134 thermodynamic properties, trace gases, and condensed species on a 26 level hybrid-sigma grid
135 extending from the surface to a constant pressure level of 2 hPa. CCSM3 has been run at a
136 variety of different horizontal resolutions for the spectral-Eulerian atmospheric dynamical core.
137 The results described here have been computed and archived at T85 resolution representing a
138 triangular truncation of the dynamics at 85 wavenumbers and corresponding to a 1.4°
139 equilateral grid on the equator. The OSSE, as described by Feldman et al. [2011a], utilises

monthly-mean values for profiles of temperature, water vapour (H_2O), carbon dioxide (CO_2), ozone (O_3), methane (CH_4), nitrous oxide (N_2O), trichlorofluoromethane (CFC-11), and dichlorodifluoromethane (CFC-12). Profiles of both liquid and ice cloud area, condensed water content, and effective radius are utilised. The treatment of cloud optics for the spectral simulations in the OSSE is identical to that used by the CCSM3. In the shortwave, the optical properties of liquid and ice clouds vary with wavelength [Hansen and Travis, 1974; Slingo, 1989]. In the longwave, liquid and ice clouds are treated as grey bodies where liquid clouds are assigned a constant emissivity and ice clouds are assigned an emissivity that varies with the effective radii diagnosed for the constituent ice crystals. The infrared absorption and scattering by aerosols are not included in the longwave OSSE; although the direct radiative effects of dust, sulfate, carbonaceous, and sea-salt aerosols are incorporated in the shortwave OSSE.

The treatment of the optical surface properties utilises the MODIS Bi-directional Reflectance Distribution Function [Schaaf et al., 2002] and has been critical for the realism of the shortwave OSSE [Feldman et al., 2011b] under present-day conditions. The formulation of the land-surface optical reflection reproduces the snow-free and snow-covered bidirectional reflectance properties from MODIS, and it also includes the effects of retreating snow cover on projections of the Earth's future reflectance field. The longwave portion of the OSSE treats ocean surfaces with unitary emissivity, while land surface emissivity is based on an annually-cyclic monthly-mean climatology derived from spatial and temporal binning of the MODIS Land Surface Emissivity product [Wan and Zhao-Liang, 1997]. By design, the effects of changes in sea-ice extent and snow cover are included in the OSSE calculations while the effects of future land-use and land-cover change and of changing soil moisture on near-infrared surface albedos are not.

This OSSE software framework requires multiple calls to the MODTRAN radiative transfer code and the OSSE is quite computationally expensive despite the optimised load-balancing and

166 intrinsic parallelism of the calculations. Even though it is has been run on a massively parallel
167 NASA High-End Computing (HEC) facility, the ratio of OSSE computational time to the
168 computational time to integrate the fully-coupled CCSM3 for the 21st Century is approximately
169 50:1. There are several potential methods to reduce this computational expense, which will be
170 discussed in Section 4.
171
172 In support of the IPCC Fifth Assessment Report, modelling centres have undertaken significant
173 efforts to produce a large set of model integrations for CMIP5. A similar infrastructure to the
174 CCSM3 offline hyperspectral calculations was adopted for two climate models. These models
175 were MIROC5 [Watanabe et al., 2010] and HadGEM2-ES [Jones et al., 2011], which lie on the
176 low and high end of the model range of CMIP5 equilibrium climate sensitivities at 2.72 and
177 4.59 °K/2xCO_2, respectively [Andrews et al., 2012]. Simulations were implemented for the first
178 three decades of the Representative Concentration Pathway 8.5 (RCP8.5) scenario [Van
179 Vuuren et al., 2011]. The fields necessary to perform reflectance and radiance calculations in
180 the OSSE have, unfortunately, only been archived at monthly-mean temporal resolution for this
181 scenario. Due to the nonlinearity of radiative transfer, it is challenging to validate offline OSSE
182 calculations with the reported values of albedo and OLR from these models, the latter of which
183 are based on averages of radiation calculations performed with time-steps of a few minutes.
184
185 **3. Results**
186 In order to meet the requirement for high-accuracy calculations to support both mission design
187 and climate model evaluation, there has been extensive validation performed on both the
188 longwave and shortwave OSSE calculations based on CCSM3. As a result, the radiation
189 calculations performed by MODTRAN are fully consistent with those produced by the CCSM3
190 radiation code, which itself is extensively evaluated against line-by-line models [Collins et al.,
191 2006b; Oreopoulos et al., 2010]. While the shortwave OSSE calculations from MODTRAN have

192 already been extensively validated against CCSM3 all-sky and clear-sky albedo [Feldman et al.,
193 2011a], the longwave fields are a new and critical feature to the OSSE, representing the first
194 time that the hyperspectral climate change signal has been simulated and validated across the
195 entire shortwave and longwave energy budget of the climate system.
196
197 Longwave validation of the two codes was performed using a comparison of TOA OLR.
198 Differences between the two radiative transfer schemes are less than 1% for both clear- and all-
199 sky conditions and arise from several factors. These factors include the contrasting treatments
200 of clouds as vertically extended non-isothermal layers in MODTRAN versus infinitely-thin
201 isothermal objects in CCSM3 together with the contrasting solutions to the radiative equations
202 using 8 discrete-ordinate streams in MODTRAN versus two streams in CCSM3. Figure (1a-b)
203 shows a distribution of the differences between the OLR produced by the OSSE through offline
204 calls to the CCSM3 longwave radiation code and the OLR produced from the MODTRAN
205 instrument emulator. Figure (1b) indicates the clear-sky calculations agree to better than 2
206 W/m^2. Meanwhile, the level of agreement between the all-sky OLR from CCSM3 and
207 MODTRAN is degraded relative to the clear-sky case, as shown in Figure (1a), with a mean
208 offset of 1 W/m^2 and a root-mean-square (RMS) value of 3.1 W/m^2. A closer investigation
209 revealed that the differences in the numbers of streams in the radiative solution and level-layer
210 formulation differences accounted for the all-sky discrepancies. This is consistent with the
211 performance of the shortwave reflectance component of the OSSE, though the all-sky
212 agreement between MODTRAN and the Community Atmosphere Model (CAM) component of
213 CCSM3 exhibit less spread because the level-layer formulation discrepancy affects OLR more
214 than albedo. The implication here is that details of vertical formulation of the radiative transfer
215 are critical for competent instrument simulation, especially in the LW. The agreement between
216 MODTRAN and CAM for shortwave fluxes is shown in Figure (1c) and (1d) with a mean offset of
217 around 3 W/m^2 in all-sky conditions and 1 W/m^2 for clear-sky conditions.

Globally-averaged longwave radiance and shortwave reflectance spectra are shown in Figure (2a) for both clear-sky and all-sky conditions at the beginning of the integration. This figure demonstrates many of the complementary features, due to a number of climate-relevant processes, in these two spectral ranges, including two high-transmittance features in the visible and the mid-infrared which are affected by the presence of clouds, but, as shown in Figure (2b), clear-sky and all-sky differences are of opposite sign between the visible and infrared. Additionally, the spectra indicate a role of water vapour in reducing reflectance in the near-infrared overtone absorption bands between 0.8 and 2.0 μm and producing rich spectral structure and decreased infrared radiance between 5 and 8.3 μm and 17 and 50 μm. Prominent greenhouse-gas absorption features are also indicated for CO_2, O_3, CH_4, and N_2O.

Figure (2b) shows the corresponding globally-averaged trends in shortwave reflectances and longwave radiances during the first 50 years of the A2 scenario simulation. Several prominent features can be seen. First, the shortwave reflectances generally increase with the increased aerosol loading projected for the first half of the 21st Century under both clear- and all-sky conditions, and this effect is evident at shorter wavelengths. While much of the spatial and seasonal heterogeneity in shortwave reflectance trends that was identified in Feldman et al. [2011a] is averaged out in the globally and annually averaged trends, the contrast between clear-sky and all-sky reflectance trends gives an indication of the additional increase in reflectance from clouds. Also, the complex spectral structure in the wings of the near-infrared H_2O overtone absorption bands indicates the potential for shortwave forcing of greenhouse gases, a topic that deserves greater scrutiny [Collins et al., 2006b].

Meanwhile, longwave radiances show a negative trend around 6.3 μm due to greater atmospheric water vapour, positive trends between 8 and 12 μm from higher surface skin

244 temperatures, and negative trends between 14 and 16 μm from increased absorption in the
245 wings of the mid-infrared CO_2 bands. The prescribed increases in CH_4 and N_2O produce
246 prominent negative trends around 7 μm, while increases in surface and tropospheric
247 temperature are aliased into positive trends in the H_2O mid- and far-IR bands.
248
249 Figure (3a-c) shows differences in zonally- and decadally-averaged shortwave reflectance and
250 longwave radiance spectra for clear-sky and all-sky conditions and cloud radiative effect (CRE)
251 between the decade from 2050-2059 and the first decade of the 21st Century, while Figure (3d-f)
252 show the differences between 2090-2099 and the first decade of the 21st Century. Increases in
253 anthropogenic aerosol loading between the decades of the 2000s and the 2050s result in
254 increased clear-sky reflectance at low latitudes and visible and near-infrared wavelengths during
255 that time period. Concurrent changes in the frozen surface coverage decrease reflectance at
256 higher latitudes in the window band but not in the near-infrared. Decadal differences in all-sky
257 shortwave reflectance share some similarities to decadal differences in the clear-sky shortwave
258 reflectance, but vertical striping features in the water-vapour overtone absorption bands are also
259 present and are indicative of the decrease in low-level stratus clouds. Additionally, movement
260 of the InterTropical Convergence Zone (ITCZ) produces a dipole in reflectance near the equator
261 with diminished striping features across the overtone absorption bands.
262
263 The changes in both all-sky and clear-sky longwave radiance exhibit the spectral features
264 highlighted in Figure (2b). The only other prominent feature is the polar amplification of surface
265 temperature warming that produces meridional gradients in the window band. Increased cloud
266 cover at high northern latitudes over this period lead to decreases in the radiance across the
267 longwave spectrum. Additionally, the stratospheric cooling and increased CO_2 are prominent
268 around 15 μm while increasing CH_4 and N_2O produce significant signals around 7 μm.
269

Differences in zonally- and decadally-averaged shortwave reflectance and longwave radiance between the start and end of the 21st Century under the A2 emissions scenario are shown in Figure (3d-f). These spectra show decreased frozen surface extent at high latitudes in visible reflectances and increased water vapour loading leading to lower reflectances in the water vapour overtone bands and at 6.3 μm and in the far-infrared H_2O rotational band. All-sky pan-spectral simulations reveal the shifts in storm-tracks with striping features in the H_2O near-infrared overtone bands at mid-latitudes, and they reveal a stronger dipole near the ITCZ near the equator across the shortwave and longwave.

The CRE changes in Figure (3c) and (3f) reveal that significant changes in low-clouds at high latitudes that impact shortwave reflectance and, to a lesser extent, longwave radiance in both panels. Movement of the ITCZ by the 2090s produces a broadband increase in shortwave reflectance but a broadband decrease in longwave radiance as shown in Figure (3f). Such features are much less apparent in the Figure (3c).

OSSEs can also be used for inter-model comparisons. To demonstrate this, we considered the contributions of the MIROC5 and HadGEM2-ES models to the CMIP5 archive. Trend differences in albedo and OLR are shown in Figure (4a-d). In all-sky OLR, as shown in Figure (4b), trend differences indicate model disagreement in deep convective response in the Tropical Western Pacific, with HadGEM2-ES showing increased deep convection as compared to MIROC5, though the difference in the trends changes sign over South America. The clear-sky OLR trend differences, as shown in Figure (4d) are small, but spatially expansive and are due in large part to the water vapour response both in convective and subsidence regions. The MIROC5 model exhibits a water vapour loading response that impacts OLR more than the HadGEM2-ES model.

For climate sensitivity, however, the difference in the processes that affect shortwave radiation of these models is larger than the longwave. Differences in the models' description of sea-ice loss and cloud response at high latitudes and particularly in subsidence regions, have been shown to contribute most significantly to the discrepancy in their equilibrium sensitivities [Andrews et al., 2012]. Hyperspectral longwave simulations based on these models have been validated with a bias of 3 W/m^2 and an RMS difference of 0.5 and 3 W/m^2 for clear-sky and all-sky longwave, respectively, with respect to the model-reported TOA fluxes. For the shortwave simulations, the hyperspectral simulations exhibit an average bias of 0.1% and an RMS difference of 1.5% and 2.2% for clear-sky and all-sky, respectively, for both models subject to the above-mentioned issues with temporal averaging. Nevertheless, Figures (4e) and (4f) indicate that there are numerous differences in the models' response in hyperspectral simulations in subsets of the OSSE spectra from the Arctic and the Tropical Western Pacific. Both the visible and infrared window spectral regions readily differentiate the two climate model runs, and spectral trends of the model differ significantly. Also, in the TWP, the sign of the change in the shortwave visible differs from that of the near-infrared water vapour overtone regions, potentially improving signal detectability, and indicating the potential for spectra to identify processes that contribute to different trends in OLR and albedo. The corollary of this is that long-term spectral trends from measurements can be confronted with the results of a hyperspectral simulator from models to exclude one or more model descriptions of the response to known forcings. It is worth noting that Huang and Ramaswamy [2009] showed that longwave spectral radiance measurements can disclose detailed climate change signals that would have otherwise been hidden in the model-reported broadband fluxes due to compensating effects. The results here also suggest that such compensation may be occurring in the shortwave as well.

One important caveat to these results, though, is, as mentioned above, the use of monthly-mean profiles for simulation. Previous work by Huang and Ramaswamy [2009] found that calculations based on monthly-mean profiles rather than instantaneous ones could introduce negative brightness temperature biases between 3 and 4 °K. To test the effect in the shortwave, we modified CCSM such that it reported the fields necessary for the OSSE at 3-hour intervals for a single month, and then compared the results from the OSSE based on a monthly-mean profile. We find that the use of monthly mean profiles leads to a positive shortwave reflectance bias RMSE of 0.05, due to the effect from clouds, but, as was found previously by Roberts et al, [2011], does not appear to impact variability significantly. However, this shortwave is larger than the climate change signal, and modelling centres therefore need to archive the fields necessary for instantaneous radiative transfer calculation to avoid precluding offline diagnoses.

Hyperspectral instrument simulators such as the one presented here enable researchers to explore the spectral dimension of climate change to understand how various processes contribute to changes in albedo and OLR. The large number of data points generated by this pan-spectral OSSE provide numerous opportunities for measurement-model intercomparison, and the contrasting performance of the OSSE in the visible and infrared windows and near-infrared water vapour overtone bands and mid-infrared vibration-rotation bands provide an indication for the potential benefit for the construction of combined shortwave and longwave spectral fingerprints (e.g., [Leroy and Anderson, 2010], [Huang et al. 2010b]) of climate change, without the degeneracy of signals from low-clouds and surface temperature.

4. Computational Expense

The computational expense of the OSSE described here is extreme, even for advanced supercomputers, and requires a careful consideration of system queuing priorities to balance

346 throughput with resource request size. Furthermore, even the expense of the COSP simulators,
347 which is considerably less than the OSSE described herein, is prohibitive.
348
349 For reference purposes, we find that, using MODTRAN, for a 26-level atmosphere, each all-sky
350 shortwave spectrum calculation, which includes 16 sub-column calls for the cloud overlap
351 approximation, requires 184 CPU-seconds while each longwave spectrum calculation, which
352 also includes 16 sub-column calls, requires 17.6 CPU-seconds on the NASA HEC resources.
353 The computational expense scales with the number of levels and sub-column calls. More
354 optimized radiative transfer codes such as Principal Component Radiative Transfer Model
355 (PCRTM) [Liu et al. 2006] can achieve a speed-up of at least an order of magnitude in the
356 shortwave and two orders of magnitude in the longwave.
357
358 In preparation for the large number of simulations that will likely be submitted to the CMIP6
359 archive, there is, a pressing need to consider how observational simulators can have reduced
360 computational expense. We therefore consider how future OSSEs may perform spatial sampling
361 to achieve tolerable radiometric accuracy with fewer radiative transfer calls. Figure (5a-d) show
362 that global and regional averages can be obtained by randomly sampling grid boxes and then
363 performing radiative transfer calculations. This will produce a level of radiometric error that is
364 less 2% for global average and 1% for Tropical Western Pacific regional average, which is
365 consistent with the CLARREO mission specification [Wielicki et al. 2013] with two orders of
366 magnitude fewer calculations. These results imply that inline satellite simulation, may be
367 tractable for CMIP5 and CMIP6 models where climatological averages are desired.
368
369 **5. Discussion**
370 This paper has introduced a software framework that is capable of simulating the shortwave and
371 longwave TOA spectral signatures of the climate change diagnosed from projections from global

climate and Earth system models. This represents a contribution to the growing literature around instrument emulation since attainment of this consistency requires particular attention to, and extensive validation of, the issues of consistent treatment of cloud overlap / geometry, cloud condensate, the spectral optical properties of cloud condensate, and the cloud thermodynamic state.

The reason why this consistency is critically important is that departures of the hyperspectral simulated signal against observations (e.g., SCIAMACHY and AIRS) can then be used directly to check the cloud physics in the model, and in turn we can examine whether broadband cloud feedbacks to climate change have a particularly large AND UNIQUE spectral signature that would be particularly useful for early-detection efforts.

The pan-spectral simulations span from the near-UV to the far-infrared and indicate a rich level of information content. Long-term measurements of changes in these quantities will capture many of the climate change processes and the relationships between these processes that are sources of uncertainty in climate models. They also indicate that the shortwave measurements are much more spatially heterogeneous than the longwave measurements, so analysis of globally-averaged changes in shortwave spectra is less suited towards diagnosing the processes that contribute to spectral changes than detailed examination of spatially resolved differences.

The ultimate goal of this research is to understand both how climate change alters the evolution of the Earth's top-of-atmosphere shortwave reflectance and longwave radiance spectra and determine whether spectral measurements enhance our detection and attribution of climate change. The pan-spectral OSSE described here will enable formal comparisons between models and a broad suite of planned and existing instrumentation, and will help establish

observational metrics for differentiating between climate models according to specific processes. This may also enhance the current efforts to utilise the highly-regularised climate model reporting framework of the CMIP5 to simulate specific instrumentation through the Observational Simulator Package (COSP) [Bodas-Salcedo et al., 2011]. As of this writing, the COSP framework (version 1.3.1) currently has an ISCCP, MODIS, CloudSat, and CALIPSO instrument emulators. It can be linked with the Radiative Transfer for Television Infrared Observation Satellite Operational Vertical Sounder (RTTOV) [Saunders et al., 1999], which is a hyperspectral mid-infrared simulator, but that package has only been developed for clear-sky applications. Regardless, is a critical need to develop the methodology to utilise the spectral dimension to gauge model performance. Recent works by Roberts et al. [2011; 2013] provide a path forward for how this can be undertaken quantitatively using principal components, and these tools may be helpful for the modelling community for narrowing the range in reported shortwave feedback.

A primary challenge to the utilisation of instrument simulators for model and measurement-model intercomparison is their large computational expense. For pan-spectral simulators, the expense is even more significant, with over 70% arising from the shortwave simulation. However, it should be noted that we found a contrast between the visible and near-infrared response to climate change, with the former largely controlled by spectrally-flat features and the latter controlled by the interaction between clouds, aerosols, water vapour, and greenhouse gases. Spectral resolution is required to capture those interactions in the near-infrared. Moreover, Roberts et al. [2011] showed that the principal component spectrum from SCIAMACHY measurements changed significantly between 25 and 100 nm Full-Width Half Max (FWHM) resolution, suggesting that information about shortwave processes requires dozens of channels, but not thousands. The computational expense can be lowered with ultra-fast radiative transfer methods (e.g., Liu et al. [2006]). Alternatively, regional calculations may be

424 considered for addressing those regions that contribute most significantly to climate sensitivity
425 divergence [Armour et al., 2013]. We also demonstrate that global and regional averages can
426 be obtained with acceptable levels of radiometric error via simulations based on random grid-
427 box sampling. This approach does have the potential to encompass a large number of existing
428 and proposed measurement concepts. It is much more of a challenge to use narrow-band
429 simulators to explore the value of new mission concepts.
430
431 For competent simulation, it is critical that model intercomparison projects, such as those of
432 CMIP5, archive the fields necessary to perform offline diagnostic radiative transfer across the
433 electromagnetic spectrum. This includes the three-dimensional thermodynamic, gaseous, and
434 condensate structure of the atmosphere, and land emission and reflectance at time-scales sub-
435 daily time-scales. The Cloud Feedback Model Intercomparison Project [Bony et al., 2011]
436 archived these fields for snapshots of several experiments associated with CMIP5, but the level
437 of participation by the modelling centres was less than for the CMIP5 Tier 1 experiments
438 including RCP8.5.
439
440 Spectra can be a very important tool for measurement model intercomparison, but OSSE
441 development needs to be expanded to consider existing hyperspectral data records, which
442 contain numerous indicators of processes that control the Earth's energy balance. As of the
443 writing of this paper, the data record from AIRS is over 11 years' long, the IASI record is over 7
444 years' long, and the SCIAMACHY record is over 10 years' long. These decadal length records
445 provide an opportunity to test present day climate model performance in multiple ways that
446 cannot be easily be adjusted with problematic tuning [Mauritsen et al., 2012] and can therefore
447 be strict constraints for model development and testing. However, the challenges that have
448 faced other long-term satellite data record analyses [Norris, 2007; Clement et al., 2009; Spencer
449 and Christy, 1992; Fu and Johanson, 2004; Seidel et al., 2011] must be considered. While orbit

and calibration are considerably less problematic for newer instrumentation, the climate quality of the instantaneous retrievals must be established. This pan-spectral simulation capability may also be applicable to recent efforts by CLARREO and GEO-CAPE to develop the pan-spectral measurements in order to answer questions related to the processes that contribute to TOA atmospheric energetics and also the evolution of tropospheric chemistry.

The community should consider how the advent of pan-spectral measurements may have the potential to detect climate change and to distinguish which climate models produce more realistic projections, sooner than is possible with conventional broadband instruments [Feldman et al., 2013]. Spectral Empirical Orthogonal Functions may accelerate this ability to distinguish models even further by exploiting spectral redundancy to minimise noise and discern spectral multi-pole features less readily detected with broadband instruments. Pan-spectral techniques can then be used to detect low-cloud feedbacks sooner and with greater accuracy than broadband or spectral infrared techniques alone. Optimal detection techniques [e.g., Newchurch et al., 2003; Leroy and Anderson, 2010] are critical to establishing how the hyperspectral dimension can be utilised to detect climate change and assess models.

Acknowledgements

Funding for this research was supported by NASA grants NNX10AK27G, and NNX11AE65G and NASA High-End Computing grants SMD-08-0999, SMD-09-1397, and SMD-10-1799. This work was also supported by Contractor Supporting Research (CSR) funding from Berkeley Lab, provided by the Director, Office of Science, of the U.S. Department of Energy under Contract No. DE-AC02-05CH11231. The following individuals also contributed: David Young, Bruce Wielicki, and Rosemary Baize of the NASA Langley Research Center, Tsengdar Lee of the NASA Science Mission Directorate, Lex Berk of Spectral Sciences, Inc., and four anonymous reviewers.

References

Andrews, T., Gregory, J. M., Webb, M. J., & Taylor, K. E. (2012). Forcing, feedbacks and climate sensitivity in CMIP5 coupled atmosphere‐ocean climate models. *Geophysical Research Letters*, *39*(9).

Armour, K. C., Bitz, C. M., & Roe, G. H. (2013). Time-Varying Climate Sensitivity from Regional Feedbacks. *Journal of Climate*, *26*(13).

Arnold, C. P., Jr. and C. H. Dey (1986), Observing-systems simulation experiments: Past, present, and future, *Bulletin of the American Meteorological Society,* 67, 687-695.

Aumann, H. H., Chahine, M. T., Gautier, C., Goldberg, M. D., Kalnay, E., McMillin, L. M., Revercomb, H., Rosenkranz, P., Smith, W., Staelin, D., Strow, L., Susskind, J. (2003). AIRS/AMSU/HSB on the Aqua mission: Design, science objectives, data products, and processing systems. *IEEE Transactions on Geoscience and Remote Sensing, 41*(2), 253-264.

Berk, A., Anderson, G. P., Acharya, P. K., Bernstein, L. S., Muratov, L., Lee, J., ... & Lewis, P. E. (2005, June). MODTRAN 5: a reformulated atmospheric band model with auxiliary species and practical multiple scattering options: update. In *Defense and Security* (pp. 662-667). International Society for Optics and Photonics.

Bodas-Salcedo, A., et al. (2011), COSP: Satellite simulation software for model assessment. *Bulletin of the American Meteorological Society*, 92, 1023–1043.

Bony, S., Webb, M., Bretherton, C., Klein, S. A., Siebesma, P., Tselioudis, G., & Zhang, M. (2011). CFMIP: Towards a better evaluation and understanding of clouds and cloud feedbacks in CMIP5 models. *Clivar Exchanges*, *56*(2), 20-22.

Bovensmann, H., Burrows, J. P., Buchwitz, M., Frerick, J., Noël, S., Rozanov, V. V., Chance, K. V., Goede, A. P. H. (1999). SCIAMACHY: Mission objectives and measurement modes. *Journal of the Atmospheric Sciences*, *56*(2), 127-150.

500 Clement, A. C., Burgman, R., & Norris, J. R. (2009). Observational and model evidence for
501 positive low-level cloud feedback. *Science*, *325*(5939), 460-464.
502 Collins, W.D. et al. (2006a), The Community Climate System Model: CCSM3. *Journal of Climate*,
503 19, 2122 – 2143.
504 Collins, W. D., Ramaswamy, V., Schwarzkopf, M. D., Sun, Y., Portmann, R. W., Fu, Q.,
505 Cassanova, S.E.B., Dufresne, J.-L. , Fillmore, D.W., Forster, P.M.D., Galin, V.Y., Gohar, L.K.,
506 Ingram, W.J., Kratz, D.P., Lefebvre, M.-P., Li, J., Marquet, P., Oinas, V., Tsushima, Y.,
507 Uchiyama, T., Zhong, W. Y. (2006b). Radiative forcing by well‐mixed greenhouse gases:
508 Estimates from climate models in the Intergovernmental Panel on Climate Change (IPCC)
509 Fourth Assessment Report (AR4). *Journal of Geophysical Research: Atmospheres (1984–*
510 *2012)*, *111*(D14).
511 Feldman, D. R., et al. (2011a), CLARREO shortwave observing system simulation experiments
512 of the twenty-first century: Simulator design and implementation, *Journal of Geophysical*
513 *Research-Atmospheres,* 116, D10107, doi:10.1029/2010JD015350.
514 Feldman, D. R., et al. (2011b), Simulation studies for the detection of changes in broadband
515 albedo and shortwave nadir reflectance spectra under a climate change scenario, *Journal of*
516 *Geophysical Research-Atmospheres*, 116, D24103, doi:10.1029/2011JD016407.
517 Feldman, D.R., D.M. Coleman, W.D. Collins, (2013), On the Usage of Spectral and Broadband
518 Satellite Instrument Measurements to Differentiate Climate Models with Different Low-Cloud
519 Feedback Strengths. *Journal of Climate*, doi: 10.1175/JCLI-D-12-00378.1.
520 Flato, G., J. Marotzke, B. Abiodun, P. Braconnot, S.C. Chou, W. Collins, P. Cox, F. Driouech, S.
521 Emori, V. Eyring, C. Forest, P. Gleckler, E. Guilyardi, C. Jakob, V. Kattsov, C. Reason and M.
522 Rummukainen, 2013: Evaluation of Climate Models. In: *Climate Change 2013: The Physical*
523 *Science Basis. Contribution of Working Group I to the Fifth Assessment Report of the*
524 *Intergovernmental Panel on Climate Change* [Stocker, T.F., D. Qin, G.-K. Plattner, M. Tignor,

525 S.K. Allen, J. Boschung, A. Nauels, Y. Xia, V. Bex and P.M. Midgley (eds.)]. Cambridge
526 University Press, Cambridge, United Kingdom and New York, NY, USA.

527 Fu, Q., & Johanson, C. M. (2004). Stratospheric influences on MSU-derived tropospheric
528 temperature trends: A direct error analysis. *Journal of Climate*,*17*(24).

529 Goody, R., J. Anderson, G. North, (1998), Testing climate models: An approach. *Bulletin of the*
530 *American Meteorological Society*, 79, 2541-2549.

531 Hansen, J.E., L.D. Travis. (1974), Light scattering in planetary atmospheres. *Space Science*
532 *Reviews*, 16(4), 527-610.

533 Hansen, J., L. Nazarenko, R. Ruedy, M. Sato, J. Willis, A. Del Genio, D. Kock, A. Lacis, K. Lo, S.
534 Menon, T. Novakov, J. Perlwitz, G. Russell, G. Schmidt, N. Tausnev, (2005), Earth's energy
535 imbalance: Confirmation and implications, *Science*, 208, 1431-1435.

536 Huang, Y., V. Ramaswamy, X. Huang, Q. Fu, C. Bardeen, (2007), A strict test in climate
537 modeling with spectrally resolved radiances: GCM simulation versus AIRS observations,
538 *Geophysical Research Letters*, 34, L24707, doi:10.1029/2007GL031409.

539 Huang, Y. and V. Ramaswamy (2009), Evolution and trend of the outgoing longwave radiation
540 spectrum. *Journal of Climate*, 22, 4637-4651.

541 Huang, Y., S.S. Leroy, J.G. Anderson (2010a), Determining Longwave Forcing and Feedback
542 Using Infrared Spectra and GNSS Radio Occultation, *Journal of Climate*, 23, 6027-6035.

543 Huang, Y., S. Leroy, J. Gero, J. Dykema, and J. Anderson (2010b), Separation of long- wave
544 climate feedbacks from spectral observations. *Journal of Geophysical Research-*
545 *Atmospheres*, 115, D07104, doi:10.1029/2009JD012766.

546 Jin, Z., B.A. Wielicki, C. Loukachine, T. P. Charlock, D. Young, and S. Noël, (2011), Spectral
547 kernel approach to study radiative response of climate variables and interannual
548 variability of reflected solar spectrum, *Journal of Geophysical Research-Atmospheres,* 116,

549 D10113.

550 Jones, C. D., et al. (2011). The HadGEM2-ES implementation of CMIP5 centennial simulations.
551 *Geoscientific Model Development*, *4*(3), 543-570.

552 Kay, J. E., Hillman, B. R., Klein, S. A., Zhang, Y., Medeiros, B., Pincus, R., Gettelman, A., Eaton,
553 B., Boyle, J., Marchand, R. Ackerman, T. P. (2012). Exposing Global Cloud Biases in the
554 Community Atmosphere Model (CAM) Using Satellite Observations and Their Corresponding
555 Instrument Simulators. *Journal of Climate*, *25*(15).

556 Kiehl, J. T., J.J. Hack, B.P. Briegleb (1994), The simulated Earth radiation budget of the
557 National Center for Atmospheric Research community climate model CCM2 and
558 comparisons with the Earth Radiation Budget Experiment (ERBE), *Journal of Geophysical*
559 *Research*, *99*(D10), 20,815–20,827, doi:10.1029/94JD00941.

560 Kiehl, J.T., and K.E. Trenberth (1997), Earth's annual global mean energy budget, *Bulletin of*
561 *the American Meteorological Society*, 78,197-208.

562 Leroy, S., J. Anderson, J. Dykema, R. Goody, (2008), Testing climate models using thermal
563 infrared spectra, *Journal of Climate*, 21, 1863-1875.

564 Liu, X., Smith, W. L., Zhou, D. K., & Larar, A. (2006). Principal component-based radiative
565 transfer model for hyperspectral sensors: theoretical concept. *Applied Optics*, *45*(1), 201-209.

566 Loeb, N.G., et al. (2009), Toward Optimal Closure of the Earth's Top-of-Atmosphere Radiation
567 Budget, *Journal of Climate*, 22, 748-766.

568 T.Mauritsen, B. Stevens, E. Roeckner, T. Crueger, M. Esch, M. Giorgetta, H. Haak, J.
569 Jungclaus, D. Klocke, D. Matei, U. Mikolajewicz, D. Notz, R. Pincus, H. Schmidt, L.
570 Tomassini, (2012), Tuning the climate of a global model, *Journal of Advances in Modeling*
571 *Earth Systems*, 4, M00A01, doi:10.1029/2012MS000154.

572 Meehl, G.A., et al. (2006), Climate Change Projections for the Twenty-First Century and Climate
573 Change Commitment in the CCSM3. *Journal of Climate*, 19, 2597-2616.

574 Meehl, G. A., R. Moss, K. E. Taylor, V. Eyring, R. J. Stouffer, S. Bony, and B. Stevens, (2014),
575 Climate Model Intercomparison: Preparing for the Next Phase, *Eos, Trans. AGU*, 95(9), 77.

576 Morcrette, J.-J. (1991), Radiation and Cloud Radiative Properties in the European Centre for
577 Medium Range Weather Forecasts Forecasting System, *Journal of Geophysical*
578 *Research*, *96*(D5), 9121–9132, doi:10.1029/89JD01597.

579 Nakicenovic, N. et al. (2000), *Special Report on Emissions Scenarios: A Special Report of*
580 *Working Group III of the Intergovernmental Panel on Climate Change*, Cambridge University
581 Press, Cambridge, U.K., 599 pp.

582 Norris, J. R. (2007). Observed Interdecadal Changes in Cloudiness: Real or Spurious?.
583 In *Climate Variability and Extremes during the Past 100 Years* (pp. 169-178). Springer
584 Netherlands.

585 Oreopoulos, L., & Mlawer, E. (2010). MODELING: The Continual Intercomparison of Radiation
586 Codes (CIRC) Assessing Anew the Quality of GCM Radiation Algorithms. *Bulletin of the*
587 *American Meteorological Society*, *91*(3), 305-310.

588 Pincus, R., Platnick, S., Ackerman, S. A., Hemler, R. S., & Patrick Hofmann, R. J. (2012).
589 Reconciling Simulated and Observed Views of Clouds: MODIS, ISCCP, and the Limits of
590 Instrument Simulators. *Journal of Climate*, *25*(13).

591 Roberts, Y. L., Pilewskie, P., & Kindel, B. C. (2011). Evaluating the observed variability in
592 hyperspectral Earth‐reflected solar radiance. *Journal of Geophysical Research:*
593 *Atmospheres*, 116(D24).

594 Roberts, Y., Pilewskie, P., B.C. Kindel, Feldman, D.R., W.D. Collins, (2013), Quantitative
595 Comparison of the Variability in Observed and Simulated Shortwave Reflectance, *Aerosol*
596 *Chemistry and Physics*, acp-2012-681.

Saunders, R., Matricardi, M., & Brunel, P. (1999). An improved fast radiative transfer model for assimilation of satellite radiance observations. *Quarterly Journal of the Royal Meteorological Society*, *125*(556), 1407-1425.

Schaaf, C.B., F. Gao, A.H. Strahler, W. Lucht, X. Li, T. Tsang, N.C. Strugnell, X. Zhang, Y. Jin, J.-P. Muller, P. Lewis, M. Barnesly, P. Hobson, M. Disney, G. Roberts, M. Dunderdale, C. Doll, R.P. d'Entremont, B. Hu, S. Liang, J.L. Privette, D. Roy (2002), First operational BRDF, albedo nadir reflectance products from MODIS, *Remote Sensing of Environment*, 83(1-2): 135-148.

Seidel, D. J., Gillett, N. P., Lanzante, J. R., Shine, K. P., & Thorne, P. W. (2011). Stratospheric temperature trends: Our evolving understanding. *Wiley Interdisciplinary Reviews: Climate Change*, *2*(4), 592-616.

Siméoni, D., Singer, C., & Chalon, G. (1997). Infrared atmospheric sounding interferometer. *Acta Astronautica,* 40(2), 113-118.

Slingo, A. (1989). A GCM parameterization for the shortwave radiative properties of clouds, *Journal of the Atmospheric Sciences*, 46, 1419-1427.

Space Studies Board (2007), *Earth Science and Applications from Space: National Imperatives for the Next Decade and Beyond*. National Academies Press (Washington DC), 456 pp.

Spencer, R. W., & Christy, J. R. (1992). Precision and radiosonde validation of satellite gridpoint temperature anomalies. Part II: A tropospheric retrieval and trends during 1979-90. *Journal of Climate*, *5*(8), 858-866.

Taylor, K. E., Stouffer, R. J., & Meehl, G. A. (2012). An overview of CMIP5 and the experiment design. *Bulletin of the American Meteorological Society*, *93*(4), 485-498.

Van Vuuren, D. P., Edmonds, J., Kainuma, M., Riahi, K., Thomson, A., Hibbard, K., Hurtt, G., Kram, T., Krey, V., Lamarque, J.-F., Masui, To., Meinshausen, M., Nakicenovic, N., Smith, S., Rose, S. K. (2011). The representative concentration pathways: an overview. *Climatic*

622 *Change*, *109*(1-2), 5-31.

623 Wan, Z., and L. Zhao-Liang (1997), A physics-based algorithm for retrieving land-surface
624 emissivity and temperature from EOS/MODIS data, *IEEE Transactions on Geoscience and*
625 *Remote Sensing*, 35(4): 980-996.

626 Watanabe, M., et al. (2010). Improved climate simulation by MIROC5: mean states, variability,
627 and climate sensitivity. *Journal of Climate*, *23*(23), 6312-6335.

628 Wielicki, B.A., et al. (2006), CERES radiation budget accuracy overview. Preprints, *12th Conf.*
629 *Atmospheric Radiation*, Madison, WI, Amer. Meteor. Soc., 9.1.

630 Wielicki, B. A., Young, D. F., Mlynczak, M. G., Thome, K. J., Leroy, S., Corliss, J., Anderson,
631 J.G., Ao, C., Bantges, R., Best, F., Bowman, K., Brindley, H., Butler, J.J., Collins, W.,
632 Dykema, J.A., Doelling, D.R., Feldman, D.R., Fox. N., Huang, X., Holz, R. (2013). Achieving
633 Climate Change Absolute Accuracy in Orbit. *Bulletin of the American Meteorological Society*,
634 *94*(10).

635 **Figure Captions**

636 Figure 1: (a) Histogram of all grid points for the difference in all-sky OLR calculated by the
637 CCSM radiative transfer code and by MODTRAN for the 32,768 grid boxes from an example
638 month January 2099 for the A2 simulation. Also included are the Pearson correlation coefficient
639 (r^2) and the mean (μ) and standard deviation (σ) of the differences between the two codes. (b)
640 Same as (a) but for clear-sky OLR. (c) Same as (a) but for all-sky shortwave flux. (d) Same as
641 (b) but for clear-sky shortwave flux.

642

643 Figure 2: (a) Pan-spectral composite of the globally-averaged all- and clear-sky shortwave
644 reflectance and longwave radiance from January 2000 for the A2 simulation. (b) Same as (a)
645 but showing the least-squares trends in shortwave reflectance (in reflectance units per decade)
646 and longwave radiance (in $W/m^2/sr/\mu m$/decade) between 2000 and 2050. Shading indicates
647 95% confidence interval of uncertainty in trends.

648

649 Figure 3: (a) Differences in zonally- and decadally-averaged pan-spectral clear-sky composite
650 for 2050-2059 and 2000-2009 for the A2 simulation. (b) Same as (a) but plotting differences in
651 all-sky conditions between the 2050s and the 2000s. (c) Differences in cloud radiative effect
652 (CRE) between the 2050s and 2000s. (d) Same as (a) but plotting differences between the
653 2090s and the 2000s. (e) Same as (d) but plotting all-sky conditions. (f) Same as (c) but plotting
654 differences between the 2090s and 2000s.

655

656 Figure 4: (a) Difference in all-sky shortwave TOA flux trends between HadGEM2-ES and
657 MIROC5 running the RCP8.5 scenario over the period 2005-2035. (b) Same as (a) but for
658 longwave TOA flux trends. (c) Same as (a) but for clear-sky shortwave TOA flux trends. (d)
659 Same as (a) but for clear-sky longwave TOA flux trends. (e) Pan-Spectral all-sky trends
660 shortwave reflectance and longwave radiance for the MIROC5 and HadGEM2-ES models

661 derived for the Arctic (70-90N; 0-100E) and (f) for the Tropical Western Pacific (10S-10N; 100-
662 150E).
663
664 Figure 5: (a) RMSE vs. number of randomly-sampled grid cells for January 2000 global average.
665 (b) Same as (a) but for a Tropical Western Pacific region (10S-10N; 100-150E). (c) Same as (a)
666 but for decadal average 2000-2009. (d) Same as (b) but for the decadal average 2000-2009.

Figure 1:

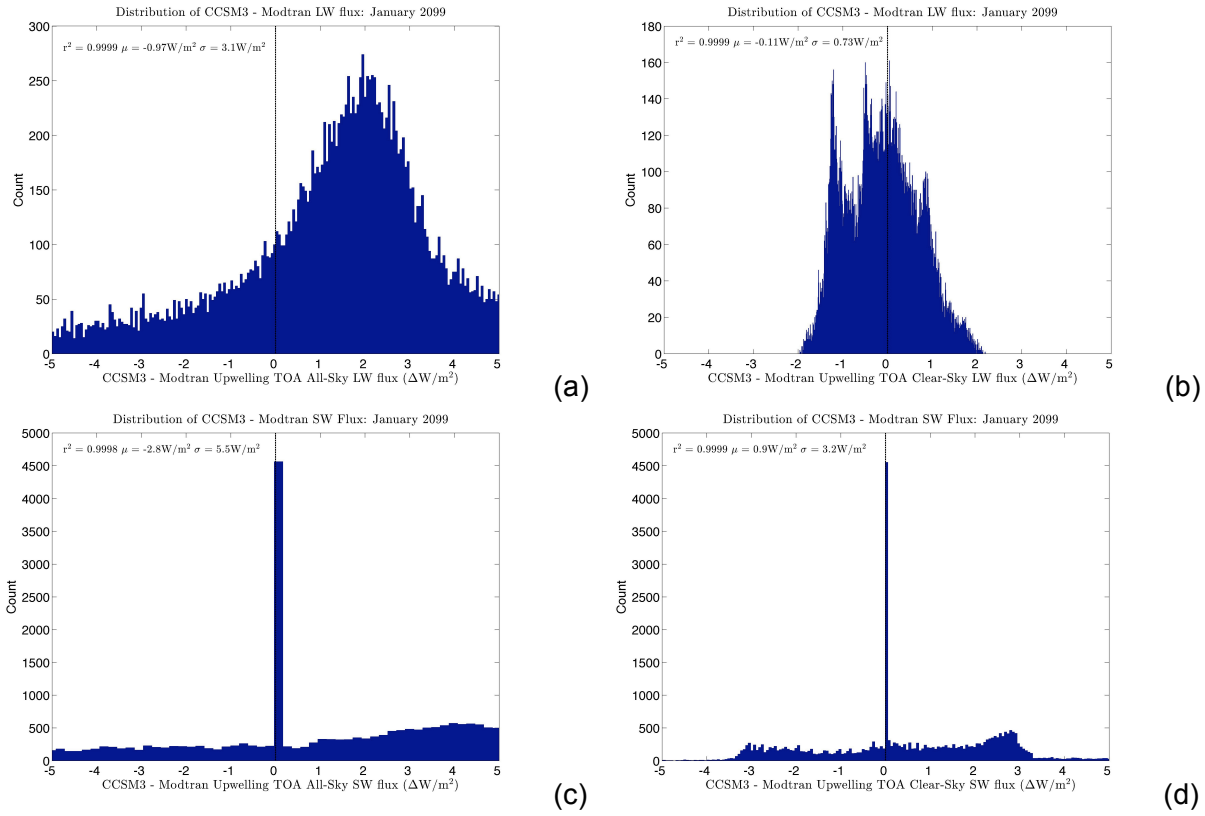
Distribution of CCSM3 - Modtran LW flux: January 2099
r² = 0.9999 μ = -0.97W/m² σ = 3.1W/m²
Count
CCSM3 - Modtran Upwelling TOA All-Sky LW flux (ΔW/m²)
(a)
Distribution of CCSM3 - Modtran LW flux: January 2099
r² = 0.9999 μ = -0.11W/m² σ = 0.73W/m²
Count
CCSM3 - Modtran Upwelling TOA Clear-Sky LW flux (ΔW/m²)
(b)
Distribution of CCSM3 - Modtran SW Flux: January 2099
r² = 0.9998 μ = -2.8W/m² σ = 5.5W/m²
Count
CCSM3 - Modtran Upwelling TOA All-Sky SW flux (ΔW/m²)
(c)
Distribution of CCSM3 - Modtran SW Flux: January 2099
r² = 0.9999 μ = 0.9W/m² σ = 3.2W/m²
Count
CCSM3 - Modtran Upwelling TOA Clear-Sky SW flux (ΔW/m²)
(d)

Figure 2:

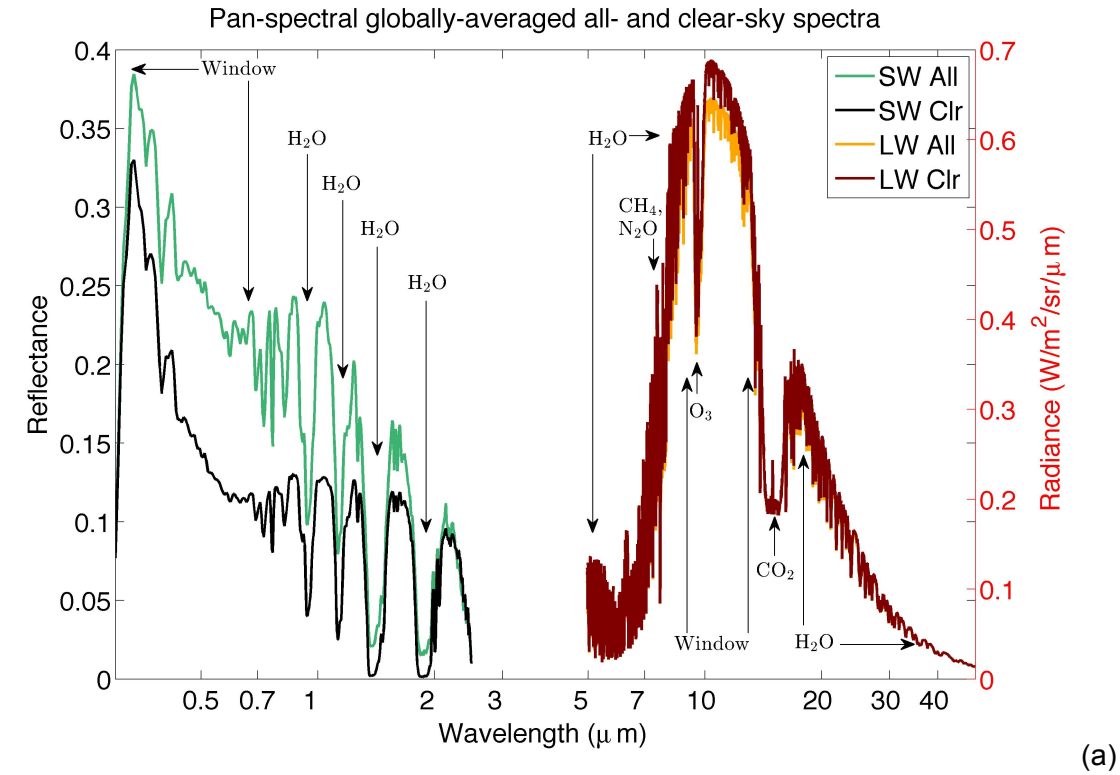
Pan-spectral globally-averaged all- and clear-sky spectra
Reflectance
Radiance (W/m^2/sr/μm)
Wavelength (μm)
SW All
SW Clr
LW All
LW Clr
Window
H_2O
CH_4, N_2O
O_3
CO_2

(a)

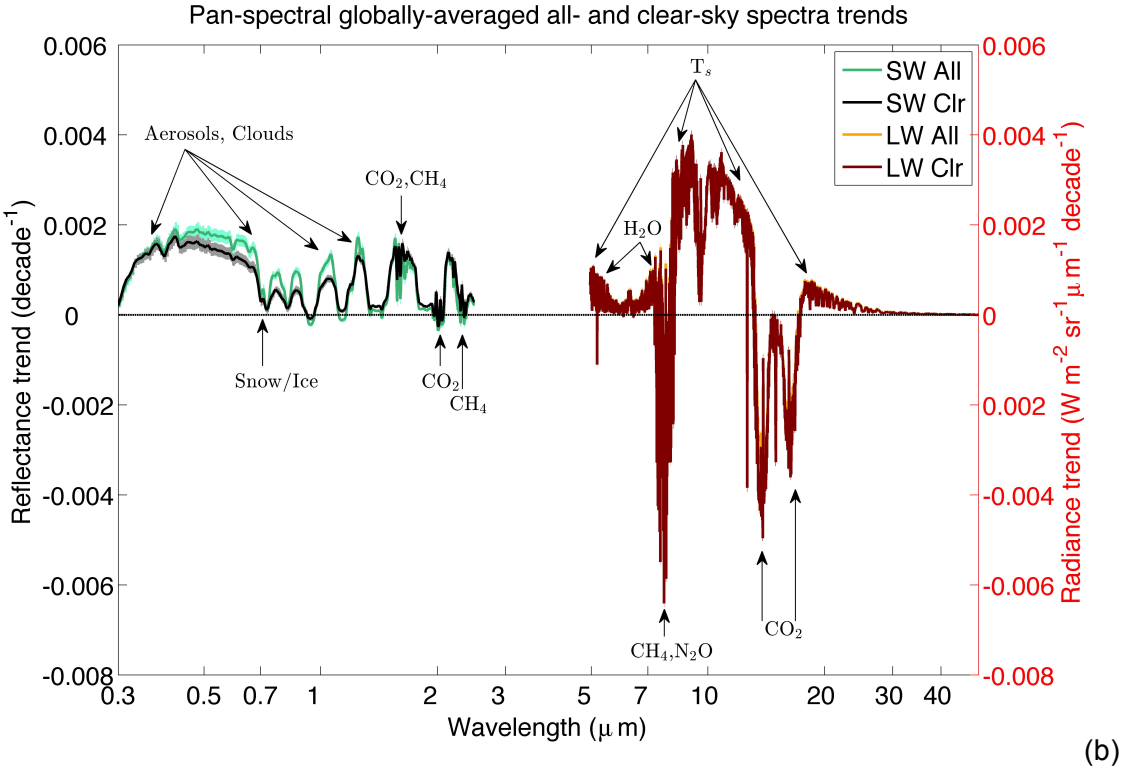
Pan-spectral globally-averaged all- and clear-sky spectra trends
Reflectance trend (decade^{-1})
Radiance trend (W m^{-2} sr^{-1} μm^{-1} decade^{-1})
Wavelength (μm)
SW All
SW Clr
LW All
LW Clr
Aerosols, Clouds
CO_2,CH_4
Snow/Ice
CO_2
CH_4
T_s
H_2O
CH_4,N_2O
CO_2

(b)

Figure 3:

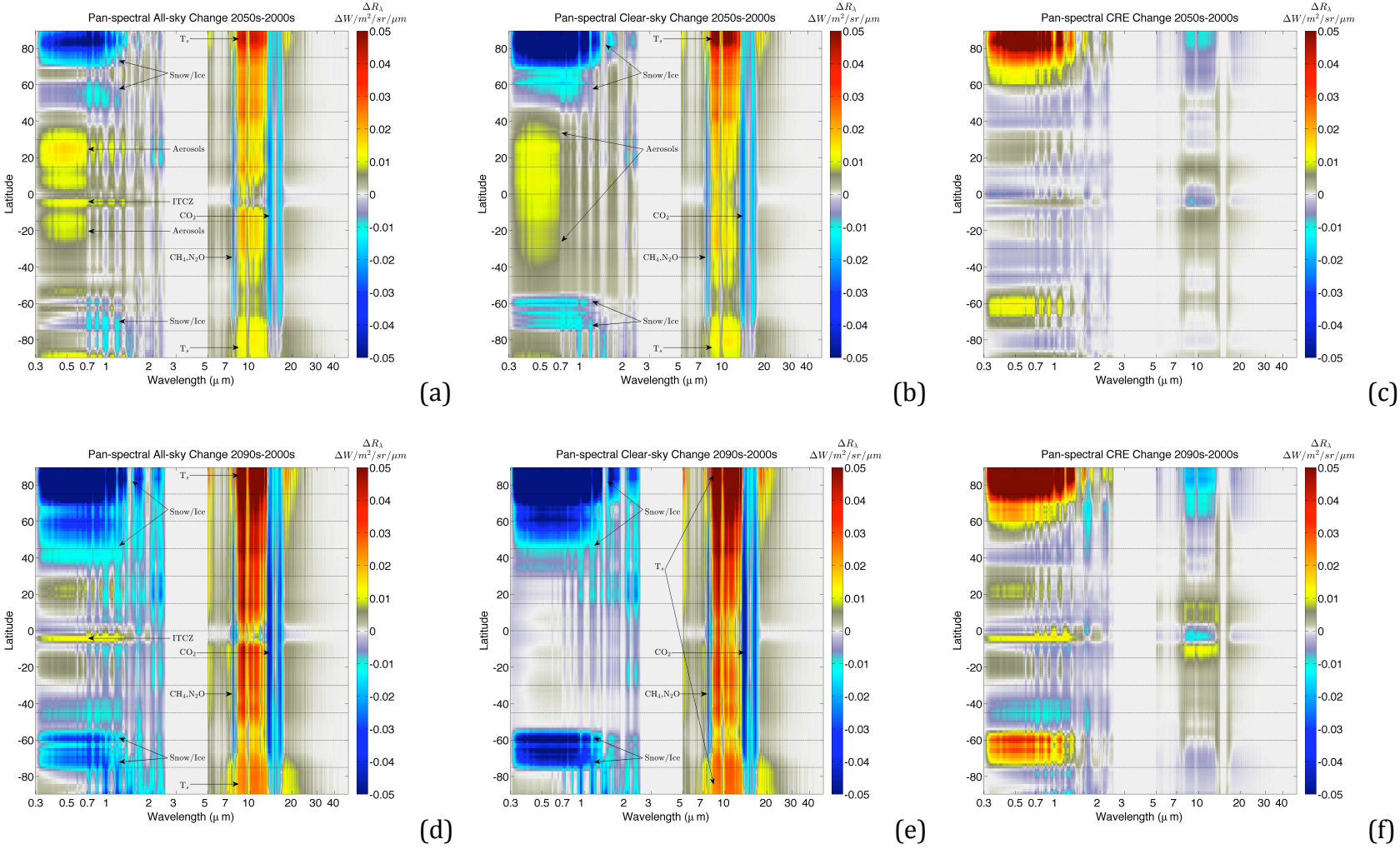
Pan-spectral All-sky Change 2050s-2000s
Pan-spectral Clear-sky Change 2050s-2000s
Pan-spectral CRE Change 2050s-2000s
Pan-spectral All-sky Change 2090s-2000s
Pan-spectral Clear-sky Change 2090s-2000s
Pan-spectral CRE Change 2090s-2000s
ΔR_λ $\Delta W/m^2/sr/\mu m$
Latitude
Wavelength (μ m)
T_s
Snow/Ice
Aerosols
ITCZ
CO_2
CH_4,N_2O
(a)
(b)
(c)
(d)
(e)
(f)

Figure 4:

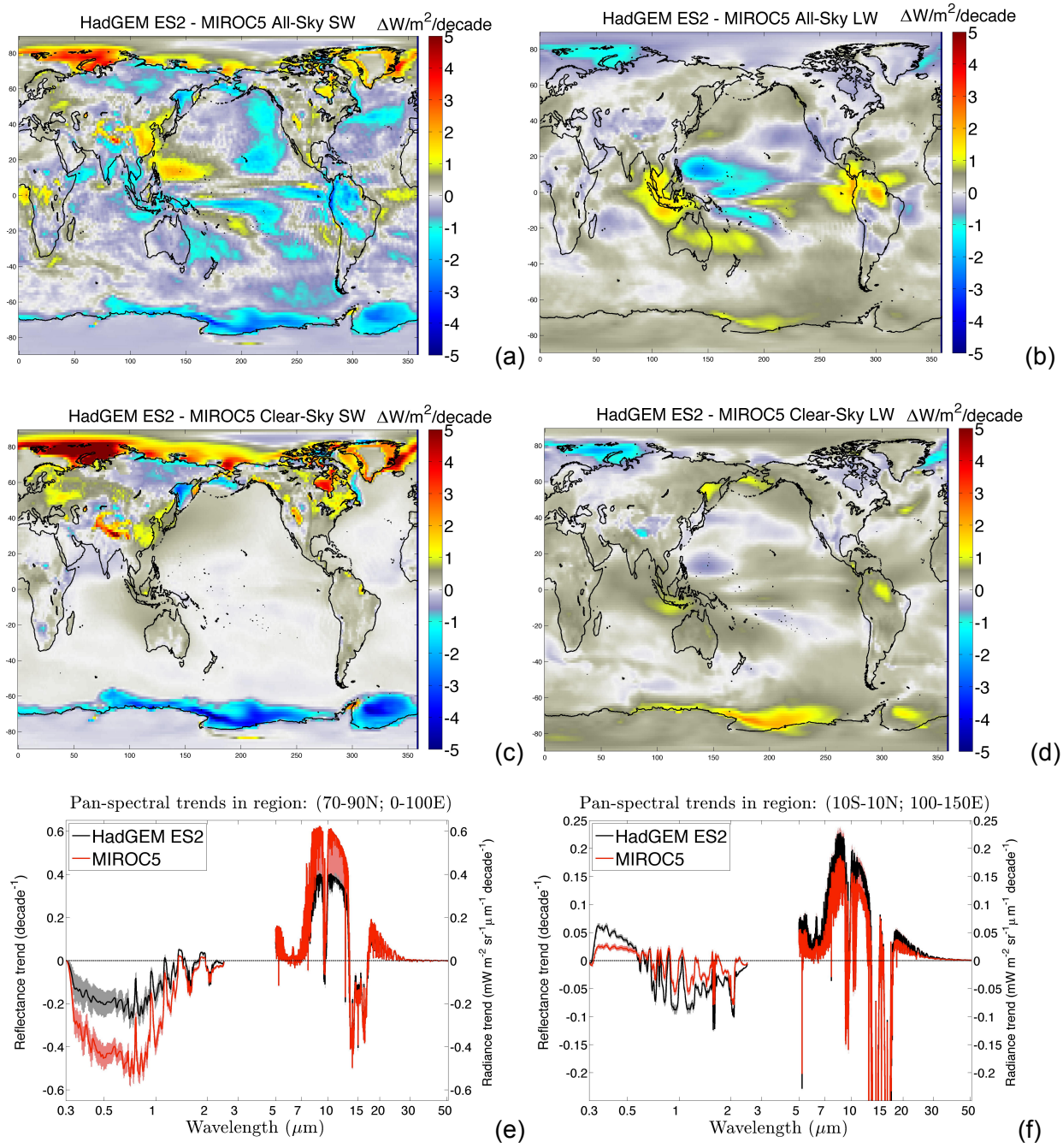
HadGEM ES2 - MIROC5 All-Sky SW ΔW/m2/decade
HadGEM ES2 - MIROC5 All-Sky LW ΔW/m2/decade
(a)
(b)
HadGEM ES2 - MIROC5 Clear-Sky SW ΔW/m2/decade
HadGEM ES2 - MIROC5 Clear-Sky LW ΔW/m2/decade
(c)
(d)
Pan-spectral trends in region: (70-90N; 0-100E)
Pan-spectral trends in region: (10S-10N; 100-150E)
HadGEM ES2
MIROC5
Reflectance trend (decade-1)
Radiance trend (mW m-2 sr-1 μm-1 decade-1)
Wavelength (μm)
(e)
(f)

Figure 5:

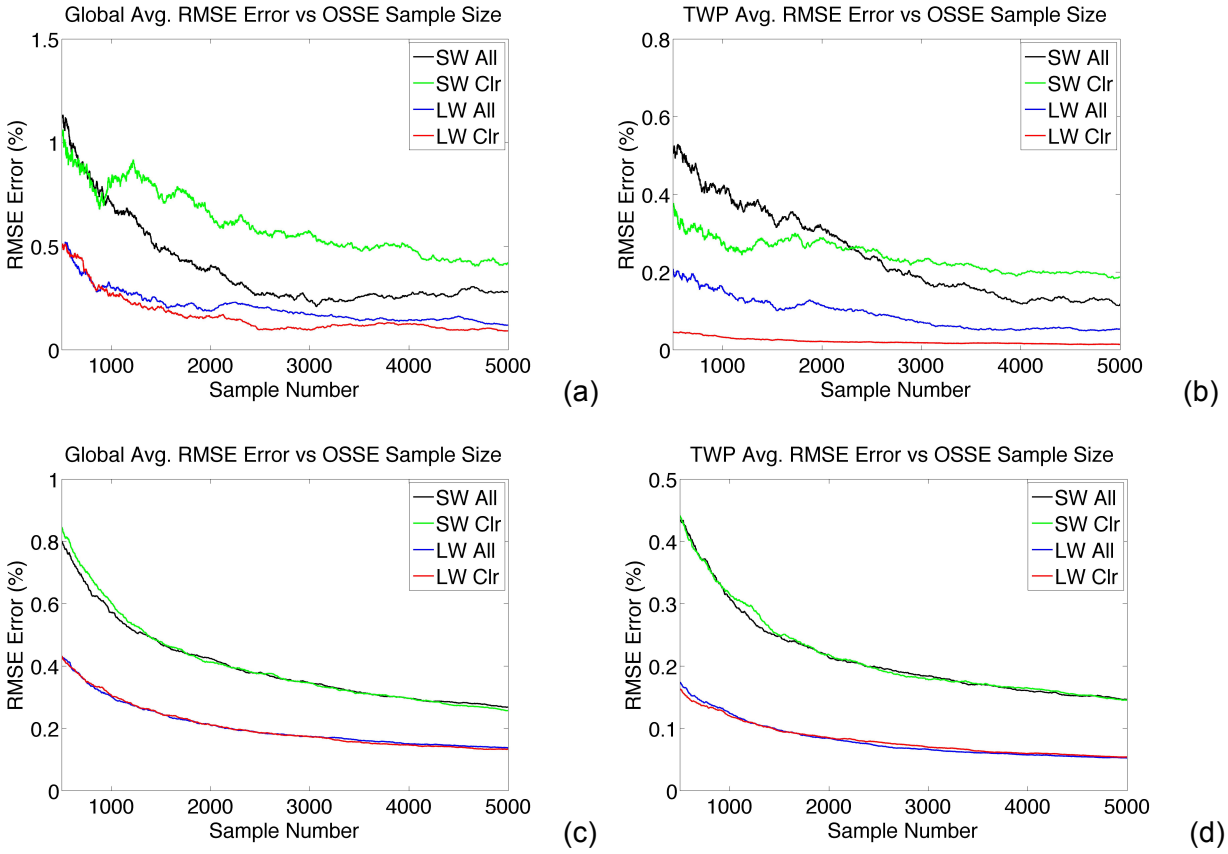
Global Avg. RMSE Error vs OSSE Sample Size
RMSE Error (%)
Sample Number
SW All
SW Clr
LW All
LW Clr
(a)
TWP Avg. RMSE Error vs OSSE Sample Size
RMSE Error (%)
Sample Number
SW All
SW Clr
LW All
LW Clr
(b)
Global Avg. RMSE Error vs OSSE Sample Size
RMSE Error (%)
Sample Number
SW All
SW Clr
LW All
LW Clr
(c)
TWP Avg. RMSE Error vs OSSE Sample Size
RMSE Error (%)
Sample Number
SW All
SW Clr
LW All
LW Clr
(d)